ACSNANO

www.acsnano.org

ARTICLE

Ultrastretchable Organogel/Silicone Fiber-Helical Sensors for Self-Powered Implantable Ligament Strain Monitoring

Feifan Sheng,[#] Bo Zhang,[#] Yihan Zhang, Yanyan Li, Renwei Cheng, Chuanhui Wei, Chuan Ning, Kai Dong,[*] and Zhong Lin Wang[*]

Cite This: https://doi.org/10.1021/acsnano.2c03365

Read Online

ACCESS | Metrics & More | Article Recommendations | Supporting Information

ABSTRACT: Implantable sensors with the abilities of real-time healthcare monitoring and auxiliary training are important for exercise-induced or disease-induced muscle and ligament injuries. However, some of these implantable sensors have some shortcomings, such as requiring an external power supply or poor flexibility and stability. Herein, an organogel/silicone fiber-helical sensor based on a triboelectric nanogenerator (OFS-TENG) is developed for power-free and sutureable implantation ligament strain monitoring. The OFS-TENG with high stability and ultrastretchability is composed of an organogel fiber and a silicone fiber intertwined with a double helix structure. The organogel fiber possesses the merits of rapid preparation (15 s), good transparency (>95%), high stretchability (600%), and favorable stability (over 6 months). The OFS-TENG is successfully implanted on the patellar ligament of the rabbit knee for the real-time monitoring of knee ligament stretch and muscle stress, which is expected to provide a solution for real-time diagnosis of muscle and ligament injuries. The prepared self-powered OFS-TENG can monitor data on human muscles and ligaments in real-time.

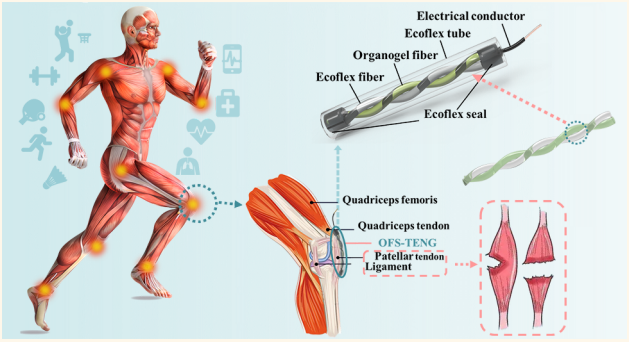

KEYWORDS: *organogel, triboelectric nanogenerators, implantations, self-powered sensors, ligament strain monitoring*

1. INTRODUCTION

The soft tissues in the ever-moving human body, such as muscles, tendons, and ligaments are easily damaged in vigorous outdoor activities.[1−3] In the absence of effective monitoring of these injuries, physical recovery may be compromised. In severe cases, bodily functions may be impaired. Therefore, sensors that can continuously monitor physical properties such as pressure and strain of human muscles and ligaments in a fast, low-cost, and straightforward manner are essential. In this way, individualized treatments can be developed for different injuries, while continuous monitoring of the mechanical behavior of tissue repair is also significant for human soft tissue rehabilitation.[4] Currently, the extent of muscles and ligaments injuries can be assessed using imaging and spectroscopy techniques in hospitals.[5,6] However, these instruments are bulky, power-wasting, and limited in continuous monitoring.[7] The desire for a better solution drives research into implantable sensors for continuous and real-time healthcare monitoring.[8]

Traditional implantable devices require surgical implantation of bulky devices and regular battery replacement.[9,10] However, rigid power modules including sensing units and control electronics may result in some mechanical mismatches between devices and body tissue. Adverse effects such as scarring or inflammation in severe cases may occur.[11−14] The operational life of an implantable sensor is usually determined by the battery life.[15,16] Therefore, self-powered methods are needed to optimize some implantable sensors.

It is necessary to choose a stretchable material to integrate the devices into soft biological structures.[17] In recent years, soft and stretchable polymeric materials have been utilized in flexible implantable sensors.[18−21] Many flexible implantable medical devices have been developed to rapidly diagnose and continuously monitor critical vital signs, which can provide

Received: April 6, 2022
Accepted: June 29, 2022

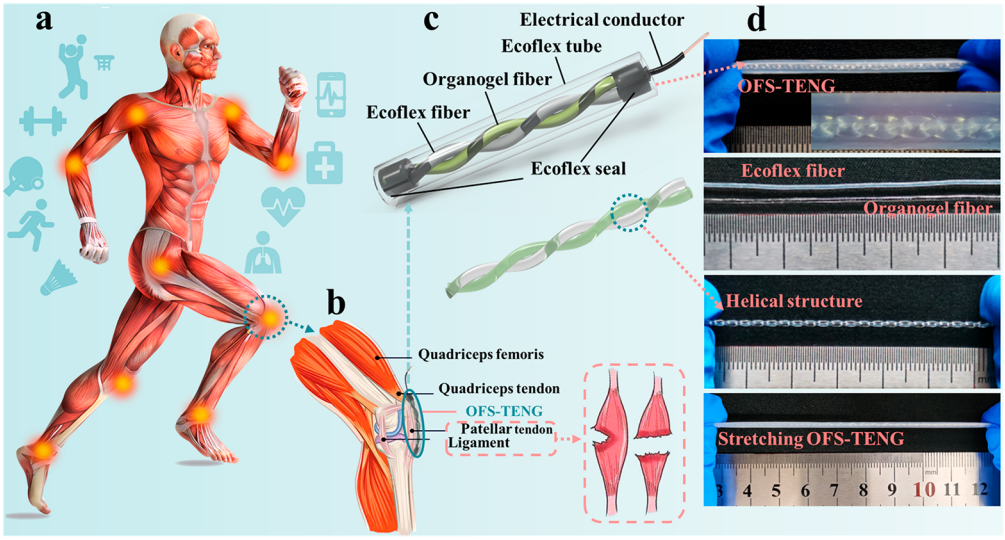

Figure 1. Application and architecture of the OFS-TENG. (a) Concept of applying OFS-TENGs implants in the human body. (b) Magnified schematic of the sensor implantable in the knee. (c) Architecture of the OFS-TENG. (d) Images of the OFS-TENG and the inner core structure and stretching.

important medical information about various related diseases.[16,22−27] However, many other challenges need to be overcome to make implantable sensors suitable for widespread applications. For example, innovations in material and device design must enable flexible implantable sensors to be volume-controllable, energy autonomous, and sutureable.[24] The accuracy and precision of the data during the measurement process also need to be improved.[28] Moreover, some concerns still exist in the cost, biocompatibility, and stability of materials.[29] Therefore, a stretchable, power-free, and stable sensor system is urgent for continuous healthcare monitoring.[30]

The triboelectric nanogenerator (TENG) originating from Maxwell's displacement currents is based on the coupling effect of triboelectrification and electrostatic induction.[31−34] It can convert external mechanical signals into electrical signals.[35,36] The wide range of material options and simple design structures of TENG provide a platform for flexible and stretchable self-powered sensors.[37,38] The selection of stable and stretchable electrodes is crucial in self-powered implantable sensors based on flexible TENG.[39] As a widely used electrode materials in flexible and stretchable TENG, ion gel electrodes exhibit both high conductivity and high stretchability.[40−44] However, most of the reported hydrogels cannot meet the long-term stability requirements due to the volatilization of water from the hydrogels, which will further degrade the performance of the devices.[40,43−46] In addition, when the hydrogel is combined with metal wires, the presence of water and oxygen can accelerate the corrosion of these metals and reduce the service life.[46] Therefore, it is necessary to design stable, stretchable, and conductive gels as the electrode for flexible and stretchable implantable sensors.

In this study, an organogel/silicone fiber-helical sensor based on TENG (OFS-TENG) with stability and stretchability are constructed for implanted real-time ligament strain monitoring. The functional organogel fiber as the electrode is obtained under ultraviolet (UV) light irradiation.[46] The preparation conditions are straightforward and fast, and the organogel has good properties. Furthermore, systematic *ex vivo* and *in vivo* tests demonstrate that the OFS-TENG is biocompatible. The OFS-TENG is successfully implanted on the patellar ligament of a rabbit knee. The output of different frequencies and bending angles is continuously monitored when the rabbit bends the knee. The OFS-TENG shows good sensitivity and stability, which provides a broad platform and prospect for implantable self-powered sensors, wearables, and health monitoring.

2. RESULTS AND DISCUSSION

2.1. Application Outlook and Architecture of the OFS-TENG. The self-powered implantable ligament strain sensor is fabricated based on the TENG technology.[47] Benefiting from the stability and stretchability of the organogel, the sensor can be well sutured to the muscles and ligaments. The movement of the muscle and ligament in the body can be monitored in real-time, which affects the rehabilitation training of the injured ligaments. Figure 1a indicates that the OFS-TENG can be used for muscle and ligament stress and stretch monitoring in various parts of the human body. As shown in the enlarged view of Figure 1b, the sensor can be implanted on the patellar ligament to output electrical signals under the movement of the human body. The sensor is compressed and stretched by the quadriceps and patellar tendons, and the quadriceps femoris and ligaments, respectively. Under the joint action of the muscle tissue, the sensor can finally obtain a real-time sensing signal which can be used to assess damage of muscle or ligament.

Figure 1 panels c and d show the detailed structural information on the OFS-TENG. The experimental section and Supporting Information, Figure S1 show the specific preparation process of the OFS-TENG. The helical inner core of the OFS-TENG consists of organogel fiber (as a conductive electrode) and silicone fiber (as a dielectric layer). The organogel and silicone fibers with the same diameter are helically wound and encapsulated in a silicone tube (eco-flex). Eco-flex is verified as the encapsulation tube due to its outstanding stretchability, good waterproofness, and biocompatibility.[24] The combined effect of triboelectrification and electrostatic induction occurs during the contact and extrusion of the two fibers inside the sensor. The movement of ligaments, muscles and soft tissue surrounding the sensor can be sensitively monitored.

2.2. Characterization of the Organogel and OFS-TENG. As an essential electrode of the OFS-TENG, a conductive,

https://doi.org/10.1021/acsnano.2c03365
ACS Nano XXXX, XXX, XXX−XXX

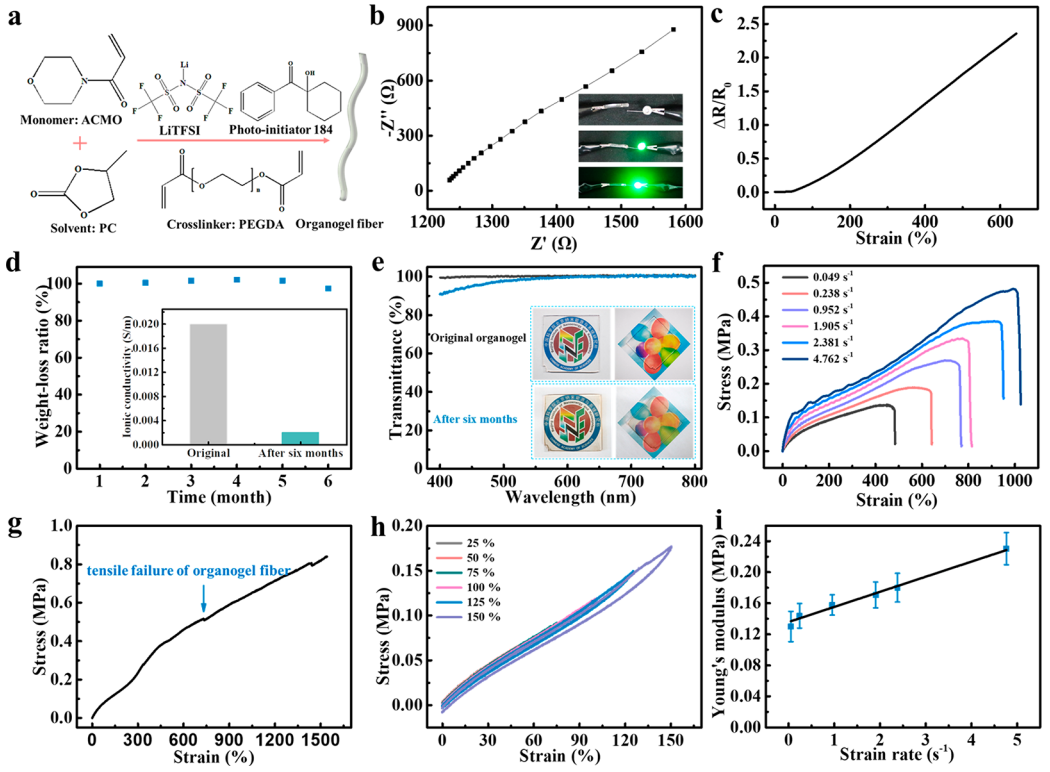

Figure 2. Characterization of the organogel and OFS-TENG. (a) Reactants required for organogel preparation. (b) Electrochemical impedance spectroscopy of organogel. Inset photograph is the conductivity of organogel. (c) Real-time resistance variation of organogel under different tensile strains. (d) Solvent retaining property of organogel after six months. The inset photo compares the conductivity of the organogel after six months. (e) A comparison of ultraviolet−visible transmittance spectra of the organogel after six months. The inset is a photo of the organogel after six months. (f) Tensile stress−strain curves at different strain rates of the organogel. (g) The tensile curve of the OFS-TENG. Arrow indicating part is the tensile failure of organogel fiber inside the OFS-TENG. The stretching rate is fixed at 50 mm min^{-1}. (h) Loading−unloading tensile curves of OFS-TENG at 25−150% strains. (i) Correlation between Young's modulus and strain rate of the OFS-TENG.

stable, and ultrastretchable organogel is prepared. As shown in Figure 2a, the 4-acryloylmorpholine monomer (ACMO) and the solvent propylene carbonate (PC) are mixed in a particular proportion. Then, the mixed solution is cured in the mold by UV light irradiation (365 nm, 48 W) for 15 s after adding photoinitiator (184) and cross-linking agent (PEGDA). The addition of the ionic conductor lithium bis-(trifluoromethylsulfonyl)imide (LiTFSI) increases the conductivity of the organogel. Figure 2b shows a lower impedance of the organogel. Moreover, the insets in Figure 2b show that the organogel can act as a wire to form a complete circuit to light an LED in the presence of an external power source which also demonstrates the good conductivity of the organogel. The output stability during the stretching process of the OFS-TENG is essential. Therefore, it is necessary to monitor the real-time resistance change of the organogel under tensile strain. As shown in Figure 2c, the organogel is stretched to 600% with a resistance change rate of 2. Therefore, resistance change rate can be ignored in the human body, where the stretching range is relatively limited.[48]

Here, the organogel is used to evaluate stability of the OFS-TENG. The stability is obtained by changing the ratio of ACMO to PC and photocuring time (Figure S2a,b). As shown in Figure 2d, the change rate of organogels' solvent of propylene carbonate (water-free) content within half a year is compared. Here, the propylene carbonate is an organic solvent with a high absorption capacity for carbon dioxide.[49] The organogel can absorb the water vapor in the air.[50,51] Therefore, during the first few months, the organogel gains some weight due to the absorption of moisture and carbon dioxide from the air. In the sixth month, the water absorbed in the organogel and some solvents start to evaporate leading to a decreasing trend in the weight of the organogel. The weight can still be maintained at more than 95%. The results show that the organogel has good organic solvent retaining ability. The inset in Figure 2d shows that the conductivity of the organogel decreases about 10-fold after six months. As shown in Figure S3, the stress−strain properties of the organogels after 15 days are compared. Furthermore, the stretchability of the organogel after three months is demonstrated (Movie S1), which suggests that the mechanical properties of the organogel are relatively stable. More applications can be developed when the organogel is more transparent. Here, the transparency of the organogel is compared after half a year. The transmittance of the organogel decreases in the range of 400−550 nm (Figure 2e), which may be attributed to the photoinitiator in the organogel responding to the light below the wavelength of 400 nm. Moreover, it can be seen from the inset that the organogel has only a slight yellowing after half a year.

In practical applications, the strain rates have great influence on the Young's modulus and the strain of the organogels. Therefore, the mechanical behaviors of the organogels at different strain rates ranging from 0.049 s^{-1} to 4.762 s^{-1} are investigated (Figure 2f and Figure S4a). The Young's modulus shows an increasing trend in the strain range even at high strain rates. In other words, the tensile stress and strain of the organogel increase linearly within a specific stretching range,

https://doi.org/10.1021/acsnano.2c03365
ACS Nano XXXX, XXX, XXX−XXX

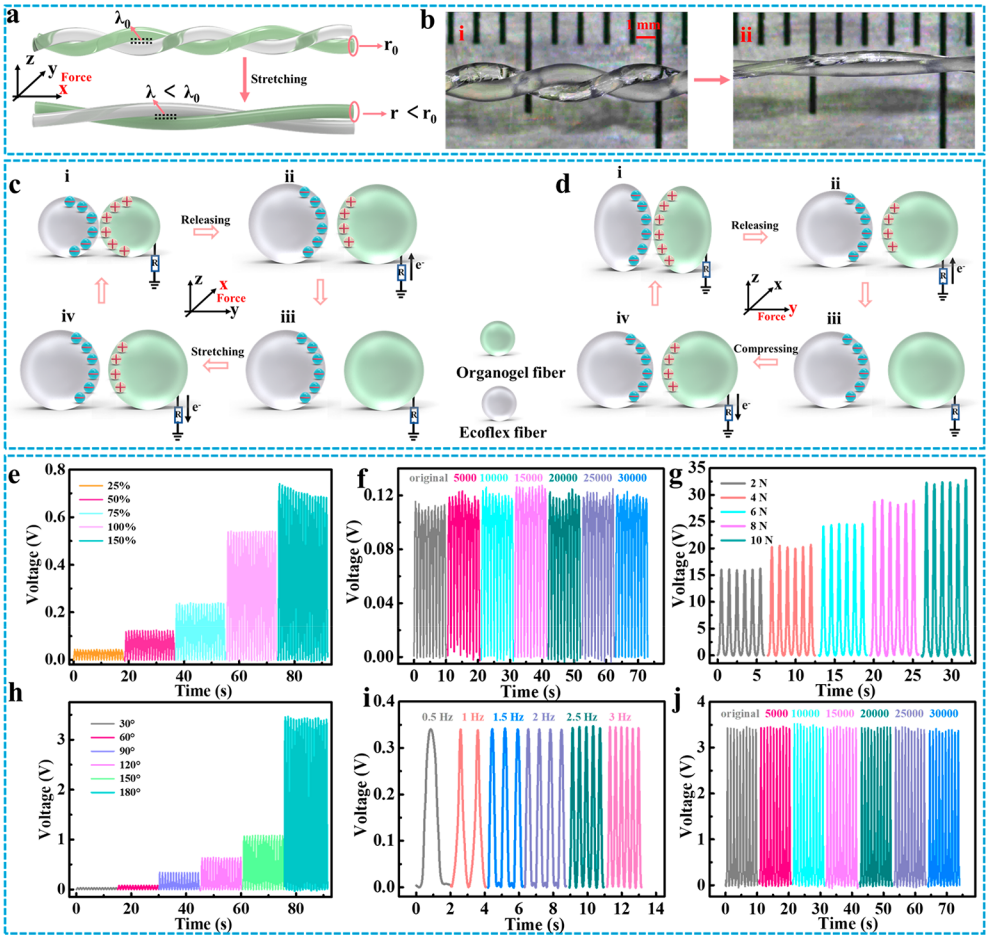

Figure 3. Mechanism and performance of the OFS-TENG. (a) Schematic diagram showing the two states of a double helix structure fibers when stretched. (b) Microscopic images of the two states of the double helix structure fibers under stretching corresponding to the fiber behaviors in panel a. Working mechanism of the OFS-TENG in stretching (c) and compressing (d) mode. (e) Output comparison of the sensor under different stretching states. (f) Stability of the OFS-TENG with stretching at 50%. (g) Different voltages of OFS-TENG under different force loads. (h) Comparison of the output of the OFS-TENG under different bending angles. (i) Output of OFS-TENG bending at 90° under different frequencies (0.5−3 Hz). (j) Stability of the OFS-TENG under the bending angle of 180°.

which indicates the obvious elastic deformation of the organogel.

As shown in Figure 2g, the mechanical properties of the OFS-TENG are investigated through the stress−strain curves. It can be seen that the fracture strain of the internal organogel is about 600% at the position marked by the arrow, which corresponds to Figure S2a. Therefore, the maximum strain of the sensor is limited at 600%. Figure 2h shows the stretching and releasing process of the sensor under different tensile strains ranging from 25% to 150% at a strain rate of 50 mm min^{-1}. The self-recovery properties of the sensor are quantitatively evaluated. It can be seen that the stretching curve of the sensor has a small hysteresis loop and can quickly return to its initial state, which verifies that the sensor has a good recovery within a specific stretching range. The strain and the Young's modulus of the OFS-TENG are verified at different strain rates stretched at 300% (Figure 2i and Figure S4b). It is proven that the sensor has good mechanical properties within a certain strain range.

2.3. Mechanism and Performance of the OFS-TENG. Figure 3 panels a−d show the interaction mechanism of the OFS-TENG during the stretching and compressing process. The OFS-TENG is stretched from the initial diameter r_0 to a certain diameter r ($r < r_0$) along the x-axis direction (Figure 3a,b and Movie S2). Moreover, the two double helical fibers are gradually straightened out and become closer to each other, which decreases the distance of the initial clearance from λ_0 to λ, finally becoming 0, as shown in Figure 3a,b (state i, ii). For better understanding, the entire stretching process is divided into three stages in more detail. The schematic diagrams of the cross-section of the two lines during the stretching process are shown in Figure S5a. The two fibers are gradually straightened and drawn closer together in the process of stretching, leading to the gradually increase of the contact area. The mechanism of the compression process is similar to the stretching process. Figure S5b shows the gradual compressive process of the two fibers along the y-axis direction. The cross-sectional area does not change (S_0), but the contact area gradually increases. To support the proposed mechanism of the force-bearing process, the pressure between the organogel and the silicon fiber is simulated by COMSOL software (Figure S6a,b).

As shown in Figure 3c,d, the mechanism of charge generation of the two operating modes is discussed. There is a small gap between the organogel fiber and the silicone fiber. As shown in Figure 3c, once the OFS-TENG is stretched to the maximum, the organogel fiber ultimately contacts with the silicone fiber, and a positive charge is generated at the interface. The same amount of negative charges in the silicone fiber are generated. Due to electrostatic balance, no electrons flow in the external

https://doi.org/10.1021/acsnano.2c03365
ACS Nano XXXX, XXX, XXX−XXX

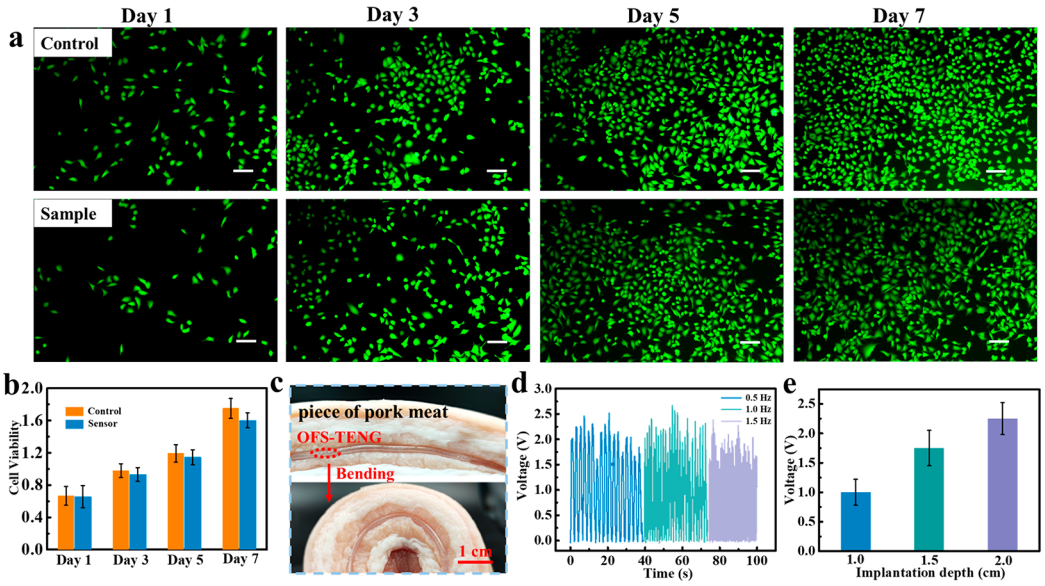

Figure 4. Biocompatibility and demonstration of the OFS-TENG *ex vivo*. (a) Fluorescence images of cardiomyocytes. Scale bars: 100 μm. (b) Cell viability of OFS-TENG for 7 days. (c) Photograph shows the OFS-TENG placed in a piece of pork. (d) Output of the embedded OFS-TENG under repeated bending and stretching cycles of the pork meat at a different frequency. (e) Output of the embedded OFS-TENG under different implanted depths.

circuit, as shown in Figure 3c(i). The eco-flex and organogel are moved away from each other after the tensile force is released. The positive charges of the conductive organogel reduce to compensate for the electrostatic charge on the silicone fiber surface, balancing the negative charge and reaching an electrical equilibrium state. During this period, electrons flow from the conductive copper wire to the organogel, generating an instantaneous current (Figure 3c, from (i) to (ii)). When the stretching state is wholly released, eco-flex and organogel are completely separate. Equilibrium is re-established, and the electrons will stop moving (Figure 3c (iii)). The positive charges induced on the copper are decreased after restretching, causing the electrons flowing to the ground (Figure 3c, from (iii) to (iv)). The OFS-TENG continuously generates alternating current by repeated stretching and releasing, resulting from the periodic operation of eco-flex and organogel contact separation process. Likewise, the working mechanism of the current generated by the compression process is similar to the stretching process (Figure 3d).

A series of optimization experiments are conducted (Figures S7–S9). Figure S7 shows that the sensors with 0, 1, 2, and 3 turns per centimeter of the two helical fibers are tested to evaluate the electrical performance according to the applied strain at 100%. The electrical performance of the sensor with 3 turns per centimeter of the two helical fibers is relatively better, which may be due to its largest effective contact area during tensile contact process. It is verified that the output of the internal fiber structure is optimal at the double helical design (Figure S8). The contact area becomes larger with an increasing diameter under the same applied load, resulting in an increased output of the OFS-TENG (Figure S9). The specific structure can be selected according to the later application and the particular implantation site. The organogel fiber with a diameter of 0.8 mm and a silicone tube with an inner diameter of 1.8 mm are chosen as the inner core and encapsulation tube of the final OFS-TENG structure for implantation into the rabbit patellar ligament.

As shown in Figure 3e, the electrical output of the OFS-TENG gradually increases as the tensile strains increase from 25% to 150%. The voltage increases from 0.05 to 0.7 V, which may be due to the contact area gradually increasing as the tensile strains increase. The electrical output of the OFS-TENG is tested to evaluate the stretched stability of the sensor. The electrical output remains stable after stretching to 50% for 30 000 cycles (Figure 3f). The electrical output of the OFS-TENG is investigated under different loading forces (Figure 3g). The electrical output shows an increasing trend with the increase of the external force. Furthermore, as shown in Figure 3h,j and Figures S13 and S14, the output and stability of the OFS-TENG under different bending angles are investigated. The primary mechanism of the OFS-TENG at a small bending angle is the tensile mode. The upper and lower tube walls with a sizable bending angle have a compressive force on the electrodes, resulting in a greater increase in electrical output. As shown in Figure 3i, there is no significant output change when the bending frequency is varied from 0.5 to 3 Hz. The stability of the sensor is tested more than 30 000 times. Figure 3j shows that the OFS-TENG still performs well even after multiple bending at 180°. The output of OFS-TENG after six months has been tested. The organogel was put at room temperature for six months, after which it was prepared and stretched at 50%, and the OFS-TENG electrical properties were tested. It can be seen from Figure S15 that the electrical output can maintain nearly 90% of its original output performance, verifying the good stability property of the organogel again.

2.4. Biocompatibility and Demonstration of the OFS-TENG *Ex Vivo*. The biocompatibility of the sensor and its electrical performance for implantation *ex vivo* is demonstrated. The proliferation of cardiomyocytes is investigated by fluorescent microscopy.[52] Figure 4a shows the fluorescent images of living cardiomyocytes that are cultured on the sensor for 1, 3, 5, and 7 days stained with FDA. The comparison chart shows that the OFS-TENG provides many adhesion sites for cells. The cardiomyocytes are adhered to the sensor surface and have a good tendency to proliferate. It can be seen that the cell

https://doi.org/10.1021/acsnano.2c03365
ACS Nano XXXX, XXX, XXX−XXX

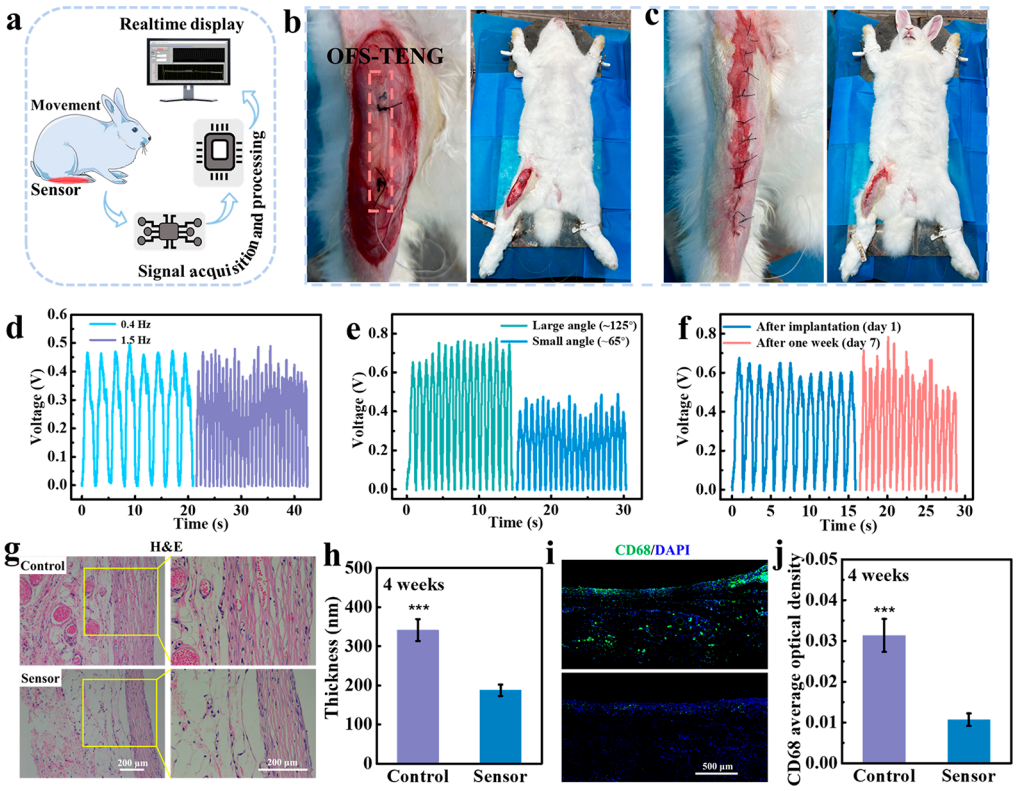

Figure 5. Application demonstration of the OFS-TENG *in vivo*. (a) Flow diagram of data acquisition and processing for strain monitoring in rabbits with the implanted sensor. (b) Photos of the OFS-TENG implanted on the patellar ligament of the rabbit knee and (c) after suturing. (d) The output of the implanted OFS-TENG under repeated bending and stretching cycles of the rabbit leg at a different frequency (~0.4 and 1.5 Hz). (e) Comparison of the output of the implanted OFS-TENG under repeated bending and stretching cycles of the rabbit leg at different bending angles. (f) Stability of the implanted OFS-TENG after 7 days. (g) Photographs and (h) quantitative analysis of H&E staining of biological tissue implanted in rabbit after 4 weeks. (i) Photographs and (j) quantitative data of immunofluorescence analysis of biological tissue implanted in rabbit after 4 weeks.

density gradually increases. The good cytocompatibility of the OFS-TENG is verified. The sensor can provide a suitable microenvironment for cell adhesion and proliferation. In addition, metabolic CCK-8 assay is further used to measure the cell proliferation of cardiomyocytes in the presence of the sensor, which further compares with that of the positive control group. As can be seen from Figure 4b, cardiomyocytes constantly proliferate well on the sensor surface within 7 days. The observation of fluorescence images and CCK-8 assay results show no cytotoxicity of the OFS-TENG.

To demonstrate the stability of the OFS-TENG in water and *ex vivo*. Figure S16 shows that the sensor has a stable voltage output underwater. The output of the sensor decreases with the increasing of depth underwater. The pressure of water only reduces the gap between the two fibers inside the sensor, resulting in that the electrical performance remains stable. The pressure on the sensor increases with the increasing of depth of the water, which gradually reduces the distance between the two friction materials inside the sensor. Therefore, the output under the same tensile force becomes smaller with the increasing of depth underwater.

As shown in Figure 4c–e, the OFS-TENG is sutured with both ends embedded in a piece of pork for the *ex vivo* demonstration. The stable sensing performance under different frequencies with the same bending angle at 60° of the pork is obtained (Figure 4d). When the pork is at the same bending angle, the bending angle of the sensor will increase with increasing implanted depth, which will result in a better performance (Figure 4e). The final output shows an increasing trend which corresponds to the results in Figure 3h. The output of the OFS-TENG embedded in a piece of pork is 2 V, and its experimental result is significantly greater than 0.08 V when compared with Figure 3h. This may occur because the sensor is completely wrapped in the pork and the internal fiber structure is subjected to compression force during the bending process. The upper and lower tube walls exerted a large compressive force on the electrodes, resulting in a sharp increase in electrical output.

2.5. Application Demonstration of the OFS-TENG *In Vivo*. The stretchability of human ligaments has a specific range (<20%),[53] and the ligaments are normal without damage within the stretched range.[24,54] The performance of ligaments can be assessed by the output of the sensor. To validate the potential of the OFS-TENG in the implantable applications, we demonstrate the ability of the OFS-TENG to monitor mechanical strains generated by the patellar ligament of a rabbit. Similar to the *ex vivo* demonstration, the output of the sensor is continuously measured during bending and stretching of the rabbit's leg. The muscle and ligament parts have compressive and tensile effect on the sensor. The sensing data processing of the OFS-TENG is shown in Figure 5a. The electrical signal is acquired and converted by the electrometer and the acquisition card, respectively. Then, the signal is adjusted and processed through the LABVIEW software to obtain a visual real-time motion data on the computer.[54,55] Thus, the stretching and stressing of ligaments can be monitored in real-time during exercise. The photographs in Figure 5 panels b and c show the

https://doi.org/10.1021/acsnano.2c03365
ACS Nano XXXX, XXX, XXX−XXX

OFS-TENG implanted and sutured on the patellar ligament of the rabbit knee, respectively. Figure 5d shows the different frequencies (~0.4 and 1.5 Hz) of the OFS-TENG under repeated stretching and bending cycles of the rabbit leg at different speeds (Movie S3). Figure 5e shows the electrical output signals obtained by the sensor with different bending angles (~125° and 65°) during repeated stretching and bending of the rabbit leg at the same speed (Supporting Information). Therefore, the degree of ligament injury can be assessed according to the output performance signals of the OFS-TENG.

The self-powered sensor exhibits stable response and good repeatability on the ligament during multiple flexion-stretching sessions. As shown in Figure 5f, the electrical output of the OFS-TENG after 7 days implantation is similar to the initial one, demonstrating the long-term stability of the OFS-TENG. As shown in Figure S17, the output of OFS-TENG decreases slightly after one month of storage in PBS buffer, demonstrating the good stability of the OFS-TENG.

The long-term monitoring and biocompatibility of the sensor are also evaluated *in vivo*. The sensors are implanted in the patellar ligament of a male New Zealand white rabbit for 4 weeks. The biocompatibility of the OFS-TENG is further performed by *in situ* signal detection. The thickness of the fibrous capsule indicates the histocompatibility and inflammatory response of the sensor.[56,57] After 4 weeks of implantation, the tissue surrounding the surface of the OFS-TENG has milder inflammatory cells infiltration and thinner fibrous capsules (187.57 ± 14.72 nm), compared with a stainless steel control group (341.27 ± 27.92 nm) according to the quantitative results of hematoxylin-eosin (H&E) staining (Figure 5g,h). In addition, the expression level of CD68 in the OFS-TENG group (0.011 ± 0.0015) is lower than that in the control group (0.031 ± 0.0040) (Figure 5i,j). The OFS-TENG shows less inflammation after one month implantation in rabbits, further demonstrating the good biocompatibility of the sensor. Therefore, our OFS-TENG has good stretchability, stability, and biocompatibility, which is available for fast real-time human−computer interaction to monitor signals of ligament stretching.

3. CONCLUSIONS

In summary, organogels with rapid preparation (15 s), good transparency (>95%), high stretchability (600%), and favorable stability (over 6 months) are developed. And a self-powered, stretchable, and stable OFS-TENG is successfully fabricated based on this functional organogel. The OFS-TENG is able to generate a stable electrical signal even in water or tissue fluid, which is successfully implanted in the patellar ligament of a rabbit's knee for real-time monitoring of cyclical ligament stretching motion. In addition, it shows stable output and biocompatibility after being kept in the rabbit body for a week. Histomorphometry analysis indicates that the OFS-TENG induces only a mild inflammation reaction and has good histocompatibility. These promising results show that the OFS-TENG has great application potential in multidirectional or multipoint ligament monitoring and rehabilitation training. We envision that the OFS-TENG can provide a meaningful approach for a smart, implantable, wireless, and self-powered sensing system if it is combined with a wireless Bluetooth low energy device.

4. MATERIALS AND METHODS

4.1. Materials. 4-Acryloylmorpholine (ACMO), propylene carbonate (PC), lithium bis(trifluoromethylsulfonyl)imide (LiTFSI), poly(ethylene glycol) diacrylate) (PEGDA), 1-hydroxycyclohexyl phenyl ketone (photoinitiator 184). All reagents were purchased from Aladdin Chemical Co., Ltd.

4.2. Preparation of Organogels. Monomer ACMO and LiTFSI's PC solution were mixed at the volume ratio of 2:1.5. LiTFSI was dissolved in solvent PC at a concentration of 0.5 M. Cross-linker PEGDA and photoinitiator 184 were then added to the mixed solution at a molar ratio of 0.1% and 1% to monomer, respectively. Precursor solution was injected into a silicon tube (diameter = 0.8 mm) after the mixed solution was thoroughly stirred. The silicon tube which contained precursor solution was cured for 15 s under a UV lamp (365 nm, 48 W) with the maximum energy, and then an organogel fiber was obtained.

4.3. Fabrication of OFS-TENG. The prepared organogel fiber and silicone fiber (Ecoflex-0010, diameter = 0.8 mm) were twisted into a spiral for 3 turns per centimeter. One copper wire was fixed at the end of the organogel. The helical fibers were put into a silicone tube (Ecoflex-0010, diameter = 2.5 mm, inner diameter = 1.8 mm, thickness = 0.5 mm, length = 3 cm), and then the fibers were pulled out of tube, and the two ends were packaged with silicone (Ecoflex-0010). The OFS-TENG device was obtained after curing (Figure S1).

4.4. Biocompatibility Experiments of the OFS-TENG. H9C2 cardiomyocytes were cultured in a DMEM medium containing 10% fetal bovine serum at 37 °C and 5% CO_2. Cells were passaged when the degree of confluency was 80% to 90%. And cells in the logarithmic growth phase were selected for experimental research. A well-biocompatible polystyrene medium-well plate was used as a positive control group to detect the cell adhesion, proliferation, and morphology of the sensor. One mL of cardiomyocytes at a concentration of 2×10^4 cells mL^{-1} were seeded onto the sensor. Cardiomyocytes were stained with fluorescein diacetate (FDA) for 5 min at room temperature after being cultured for 1, 3, 5, and 7 days. After being washed with serum-free medium, the cell adhesion was observed immediately by an inverted fluorescence microscope.

The Cell Counting Kit-8 kit (CCK-8, Japan, Dojindo; Cell Counting Kit) was used to detect the absorbance of cells at 1, 3, 5, and 7 days. The proliferation activity of cells was evaluated quantitatively. A 1 mL aliquot of cardiomyocytes with a concentration of 2×10^4 cells mL^{-1} was seeded on the sensor. The samples need to be transplanted to a new 24-well plate to avoid the cells accidentally touching the sensor and being disturbed before the experimental detection. CCK-8 (100 μL) and serum-free medium (900 μL) were added to each well and incubated at 37 °C for an additional 4 h. The absorbance value of each well at a wavelength of 450 nm was recorded by a microplate reader.

4.5. Animal Surgery and Demonstration *In Vivo*. All surgical procedures were approved according to the Animal Experiment Guidelines of Huaxi Laboratory Animal Center of Sichuan University for the care and use of animals during the experiment. New Zealand white rabbits (male; $n = 6$; age, 3 months; body weight, 2.5−3 kg) were selected for the experiment and anesthetized by ear vein injection of 3% pentobarbital (0.75 mL kg^{-1} body weight). The rabbit's knee was shaved and sterilized with iodophor and 75% alcohol. Then 0.5% lidocaine was injected locally into the knee joint tissue. A 5 mm incision was made longitudinally at 1.5 cm above the knee joint. The sensor was insert to the incision after separating the muscle tissue and fascia. The sensor and conductive wire were pulled out, and the fascia completely covered the sensor. The total depth was 7 mm. Both ends of the sensor were fixed on the tissue by degradable surgical wire, and the skin was sutured after the conductive wire on the sensor was set aside. Postoperatively, intramuscular injections of gentamicin (10 mg kg^{-1}) and penicillin sodium (10 mg kg^{-1}) were administered for 3 days.

4.6. Inflammation Response. The implant and surrounding tissue were removed and prepared for histological observation one month after surgery. The sensor samples with hyperplastic tissue were fixed in 4% paraformaldehyde for 5 days. Then, the surrounding tissue was separated from the sensor. The hyperplastic tissue was embedded with paraffin after being gradually dehydrated through a series of graded ethanolic solutions and infiltrated. Subsequently, the samples were cut to obtain sections (5 μm). Finally, the prepared sections were stained

https://doi.org/10.1021/acsnano.2c03365
ACS Nano XXXX, XXX, XXX−XXX

with H&E and CD68 to evaluate tissue biocompatibility and inflammatory response.

4.7. Statistical Analysis. All quantitative results were obtained from three independent experiments. The data were analyzed using SPSS version 11.5 and shown as mean ± standard deviation. Statistical significance was determined using a one-way analysis of variance. Differences were considered significant at $P < 0.05$ ($^{*}P < 0.05$, $^{**}P < 0.01$, and $^{***}P < 0.001$).

4.8. Characterization and Measurements. Organogels were prepared using a UV cross-linker CL-3000L (365 nm). FTIR spectra were studied in the 400−4000 cm^{-1} range using a Nicolet 5700 FTIR instrument at room temperature. The UV−vis−NIR spectra of the organogels were tested using a Shimadzu UV-3600 spectrophotometer at room temperature. Stress−strain testing of the organogel and OFS-TENG was performed using an Instron EP3000 system. All stretching rates were fixed at 50 $mm{\cdot}min^{-1}$ unless otherwise stated. Real-time resistance was collected using a precision LCR meter (KEYSIGHT E4980AL). The organogel impedance was tested using Chenhua CHI-660E electrochemical workstation. When external force drives the OFS-TENG, a linear motor (LinMot E1100) provides mechanical motion input. The electrical outputs were collected using a Keithley Electrometer 6514.

ASSOCIATED CONTENT

Supporting Information

The Supporting Information is available free of charge at https://pubs.acs.org/doi/10.1021/acsnano.2c03365.

Stretchability of the organogel after three months (MP4)

Microscopic movie of the two double helical fibers under stretching (MP4)

Application demonstration of the OFS-TENG *in vivo* (MP4)

Table S1, Figures S1−S17: Summary and comparison of helical structure TENGs; schematic diagram of the OFS-TENG preparation process; optimization process of the organogel fiber; mechanical property of the organogel and the OFS-TENG; mechanism diagram and simulation schematics of the OFS-TENG; output of different structure of the OFS-TENGs; voltage response of the OFS-TENG to different strains; response time at different frequencies; output of OFS-TENG at different bending angles; stability of the OFS-TENG; output of the OFS-TENG under water at different depth (PDF)

AUTHOR INFORMATION

Corresponding Authors

Kai Dong − *CAS Center for Excellence in Nanoscience Beijing Key Laboratory of Micro-Nano Energy and Sensor, Beijing Institute of Nanoenergy and Nanosystems, Chinese Academy of Sciences, Beijing 101400, P. R. China; School of Nanoscience and Technology, University of Chinese Academy of Sciences, Beijing 100049, P. R. China;* orcid.org/0000-0001-6314-1546; Email: dongkai@binn.cas.cn

Zhong Lin Wang − *CAS Center for Excellence in Nanoscience Beijing Key Laboratory of Micro-Nano Energy and Sensor, Beijing Institute of Nanoenergy and Nanosystems, Chinese Academy of Sciences, Beijing 101400, P. R. China; School of Nanoscience and Technology, University of Chinese Academy of Sciences, Beijing 100049, P. R. China; School of Material Science and Engineering, Georgia Institute of Technology, Atlanta, Georgia 30332, United States;* orcid.org/0000-0002-5530-0380; Email: zhong.wang@mse.gatech.edu

Authors

Feifan Sheng − *CAS Center for Excellence in Nanoscience Beijing Key Laboratory of Micro-Nano Energy and Sensor, Beijing Institute of Nanoenergy and Nanosystems, Chinese Academy of Sciences, Beijing 101400, P. R. China; School of Chemistry and Chemical Engineering, Center on Nanoenergy Research, School of Physical Science & Technology, Guangxi University, Nanning 530004, P. R. China*

Bo Zhang − *National Engineering Research Center for Biomaterials, Sichuan University, Chengdu 610064, P. R. China*

Yihan Zhang − *CAS Center for Excellence in Nanoscience Beijing Key Laboratory of Micro-Nano Energy and Sensor, Beijing Institute of Nanoenergy and Nanosystems, Chinese Academy of Sciences, Beijing 101400, P. R. China; School of Nanoscience and Technology, University of Chinese Academy of Sciences, Beijing 100049, P. R. China*

Yanyan Li − *National Engineering Research Center for Biomaterials, Sichuan University, Chengdu 610064, P. R. China*

Renwei Cheng − *CAS Center for Excellence in Nanoscience Beijing Key Laboratory of Micro-Nano Energy and Sensor, Beijing Institute of Nanoenergy and Nanosystems, Chinese Academy of Sciences, Beijing 101400, P. R. China; School of Nanoscience and Technology, University of Chinese Academy of Sciences, Beijing 100049, P. R. China;* orcid.org/0000-0002-4350-9734

Chuanhui Wei − *CAS Center for Excellence in Nanoscience Beijing Key Laboratory of Micro-Nano Energy and Sensor, Beijing Institute of Nanoenergy and Nanosystems, Chinese Academy of Sciences, Beijing 101400, P. R. China; School of Nanoscience and Technology, University of Chinese Academy of Sciences, Beijing 100049, P. R. China*

Chuan Ning − *CAS Center for Excellence in Nanoscience Beijing Key Laboratory of Micro-Nano Energy and Sensor, Beijing Institute of Nanoenergy and Nanosystems, Chinese Academy of Sciences, Beijing 101400, P. R. China; School of Nanoscience and Technology, University of Chinese Academy of Sciences, Beijing 100049, P. R. China*

Complete contact information is available at: https://pubs.acs.org/10.1021/acsnano.2c03365

Author Contributions

#F.S. and B.Z. contributed equally to this work.

Notes

The authors declare no competing financial interest.

ACKNOWLEDGMENTS

The authors are grateful for the support received from the National Key R&D Project from the Ministry of Science and Technology (Grant No. 2021YFA1201601), National Natural Science Foundation of China (Grant No. 22109012), Natural Science Foundation of the Beijing Municipality (Grant No. 2212052), the Fundamental Research Funds for the Central Universities (Grant No. E1E46805). Informed consent was obtained from the volunteers who participated in the experiments.

REFERENCES

(1) Fernández-García, J. C.; Gálvez-Fernández, I.; Mercadé-Melé, P.; Gavala-González, J. Longitudinal Study of Body Composition and

Energy Expenditure in Overweight or Obese Young Adults. *Sci. Rep.* **2020**, *10*, 5305.
(2) Cai, J.; Wang, J.; Ye, K.; Li, D.; Ai, C.; Sheng, D.; Jin, W.; Liu, X.; Zhi, Y.; Jiang, J.; Chen, J.; Mo, X.; Chen, S. Dual-Layer Aligned-Random Nanofibrous Scaffolds for Improving Gradient Microstructure of Tendonto-Bone Healing in a Rabbit Extra-Articular Model. *Int. J. Nanomed.* **2018**, *13*, 3481−3492.
(3) Mintz, E. L.; Passipieri, J. A.; Franklin, I. R.; Toscano, V. M.; Afferton, E. C.; Sharma, P. R.; Christ, G. J. Long-Term Evaluation of Functional Outcomes Following Rat Volumetric Muscle Loss Injury and Repair. *Tissue Eng. Pa. A* **2020**, *26*, 140−156.
(4) Luyckx, T.; Verstraete, M.; De Roo, K.; De Waele, W.; Bellemans, J.; Victor, J. Digital Image Correlation as a Tool for Three-Dimensional Strain Analysis in Human Tendon Tissue. *J. Exp. Orthop.* **2014**, *1*, 1−9.
(5) Hariharan, K. V.; Terhorst, L.; Maxwell, M. D.; Bise, C. G.; Timko, M. G.; Schneider, M. J. Inter-Examiner Reliability of Radiographic Measurements from Open-Mouth Lateral Bending Cervical Radiographs. *Chiropr. Man. Ther.* **2020**, *28*, 1−9.
(6) Kaminski, T. W.; Hertel, J.; Amendola, N.; Docherty, C. L.; Dolan, M. G.; Hopkins, J. T.; Nussbaum, E.; Poppy, W.; Richie, D. National Athletic Trainers' Association Position Statement: Conservative Management and Prevention of Ankle Sprains in Athletes. *J. Athl. Training* **2013**, *48*, 528−545.
(7) Lund, M.; Bjerre, T. A.; Grønbæk, H.; Mortensen, F.; Andersen, P. K. Contrast-Enhanced Ultrasound Compared with Computed Tomography, Magnetic Resonance Imaging, and Positron Emission Tomography for Diagnosing Liver Metastases in People with Newly Diagnosed Colorectal Cancer. *Cochrane Db. Syst. Rev.* **2016**, CD012388.
(8) Yu, Z.; Zahid, A.; Ansari, S.; Heidari, H.; Abbas, H.; Abdulghani, A. M.; Imran, M. A.; Abbasi, Q. H. Hardware-Based Hopfield Neuromorphic Computing for Fall Detection. *Sensors* **2020**, *20*, 7226−7241.
(9) Lee, B.; Koripalli, M. K.; Jia, Y.; Acosta, J.; Sendi, M. S. E.; Choi, Y.; Ghovanloo, M. An Implantable Peripheral Nerve Recording and Stimulation System for Experiments on Freely Moving Animal Subjects. *Sci. Rep.* **2018**, *8*, 6115−6126.
(10) Sriram, S.; Avlani, S.; Ward, M. P.; Sen, S. Electro-Quasistatic Animal Body Communication for Untethered Rodent Biopotential Recording. *Sci. Rep.* **2021**, *11*, 1−14.
(11) Joo, H.; Lee, Y.; Kim, J.; Yoo, J.-S.; Yoo, S.; Kim, S.; Arya, A. K.; Kim, S.; Choi, S. H.; Lu, N.; Lee, H. S.; Kim, S.; Lee, S.-T.; Kim, D.-H. Soft Implantable Drug Delivery Device Integrated Wirelessly with Wearable Devices to Treat Fatal Seizures. *Sci. Adv.* **2021**, *7*, No. eabd4639.
(12) Dashtimoghadam, E.; Fahimipour, F.; Keith, A. N.; Vashahi, F.; Popryadukhin, P.; Vatankhah-Varnosfaderani, M.; Sheiko, S. S. Injectable Non-Leaching Tissue-Mimetic Bottlebrush Elastomers as an Advanced Platform for Reconstructive Surgery. *Nat. Commun.* **2021**, *12*, 1−11.
(13) Choi, Y.; Park, K.; Choi, H.; Son, D.; Shin, M. Self-Healing, Stretchable, Biocompatible, and Conductive Alginate Hydrogels through Dynamic Covalent Bonds for Implantable Electronics. *Polymers* **2021**, *13*, 1133−1145.
(14) Asulin, M.; Michael, I.; Shapira, A.; Dvir, T. One-Step 3D Printing of Heart Patches with Built-in Electronics for Performance Regulation. *Adv. Sci.* **2021**, *8*, 2004205.
(15) Bhandari, S.; Bergmann, N.; Jurdak, R.; Kusy, B. Time Series Data Analysis of Wireless Sensor Network Measurements of Temperature. *Sensors* **2017**, *17*, 1221−1236.
(16) Adhikari, P. R.; Tasneem, N. T.; Reid, R. C.; Mahbub, I. Electrode and Electrolyte Configurations for Low Frequency Motion Energy Harvesting Based on Reverse Electrowetting. *Sci. Rep.* **2021**, *11*, 5030−5042.
(17) Boutry, C. M.; Kaizawa, Y.; Schroeder, B. C.; Chortos, A.; Legrand, A.; Wang, Z.; Chang, J.; Fox, P.; Bao, Z. A Stretchable and Biodegradable Strain and Pressure Sensor for Orthopaedic Application. *Nat. Electron.* **2018**, *1*, 314−321.
(18) Someya, T.; Bao, Z.; Malliaras, G. G. The Rise of Plastic Bioelectronics. *Nature* **2016**, *540*, 379−385.
(19) Liao, X.; Wang, W.; Wang, L.; Jin, H.; Shu, L.; Xu, X.; Zheng, Y. A Highly Stretchable and Deformation-Insensitive Bionic Electronic Exteroceptive Neural Sensor for Human-Machine Interfaces. *Nano Energy* **2021**, *80*, 105548.
(20) Wu, H.; Yang, G.; Zhu, K.; Liu, S.; Guo, W.; Jiang, Z.; Li, Z. Materials, Devices, and Systems of on-Skin Electrodes for Electrophysiological Monitoring and Human-Machine Interfaces. *Adv. Sci.* **2021**, *8*, 2001938.
(21) Mu, J.; Hou, C.; Wang, G.; Wang, X.; Zhang, Q.; Li, Y.; Wang, H.; Zhu, M. An Elastic Transparent Conductor Based on Hierarchically Wrinkled Reduced Graphene Oxide for Artificial Muscles and Sensors. *Adv. Mater.* **2016**, *28*, 9491−9497.
(22) Jin, P.; Fu, J.; Wang, F.; Zhang, Y.; Wang, P.; Liu, X.; Jiao, Y.; Li, H.; Chen, Y.; Ma, Y.; Feng, X. A Flexible, Stretchable System for Simultaneous Acoustic Energy Transfer and Communication. *Sci. Adv.* **2021**, *7*, No. eabg2507.
(23) Sekitani, T.; Yokota, T.; Kuribara, K.; Kaltenbrunner, M.; Fukushima, T.; Inoue, Y.; Sekino, M.; Isoyama, T.; Abe, Y.; Onodera, H.; Someya, T. Ultraflexible Organic Amplifier with Biocompatible Gel Electrodes. *Nat. Commun.* **2016**, *7*, 1−11.
(24) Lee, J.; Ihle, S. J.; Pellegrino, G. S.; Kim, H.; Yea, J.; Jeon, C.-Y.; Son, H.-C.; Jin, C.; Eberli, D.; Schmid, F.; Zambrano, B. L.; Renz, A. F.; Forró, C.; Choi, H.; Jang, K.-I.; Küng, R.; Vörös, J. Stretchable and Suturable Fibre Sensors for Wireless Monitoring of Connective Tissue Strain. *Nat. Electron.* **2021**, *4*, 291−301.
(25) Lee, S.; Shi, Q.; Lee, C. From Flexible Electronics Technology in the Era of Iot and Artificial Intelligence toward Future Implanted Body Sensor Networks. *APL Mater.* **2019**, *7*, 031302.
(26) Wang, X.; Liu, J. Recent Advancements in Liquid Metal Flexible Printed Electronics: Properties, Technologies, and Applications. *Micromachines* **2016**, *7*, 206−229.
(27) Keum, D. H.; Kim, S.-K.; Koo, J.; Lee, G.-H.; Jeon, C.; Mok, J. W.; Mun, B. H.; Lee, K. J.; Kamrani, E.; Joo, C.-K.; Shin, S.; Sim, J.-Y.; Myung, D.; Yun, S. H.; Bao, Z.; Hahn, S. K. Wireless Smart Contact Lens for Diabetic Diagnosis and Therapy. *Sci. Adv.* **2020**, *6*, No. eaba3252.
(28) Li, P.; Huang, L.; Peng, J. Sensor Distribution Optimization for Structural Impact Monitoring Based on NSGA-II and Wavelet Decomposition. *Sensors* **2018**, *18*, 4264−4278.
(29) Xu, S.; Jayaraman, A.; Rogers, J. A. Skin Sensors Are the Future of Health Care. *Nature* **2019**, *571*, 319−321.
(30) Cheng, M.; Zhu, G.; Zhang, F.; Tang, W.-L.; Jianping, S.; Yang, J.-Q.; Zhu, L.-Y. A Review of Flexible Force Sensors for Human Health Monitoring. *J. Adv. Res.* **2020**, *26*, 53−68.
(31) Zhang, R.; Dahlstrom, C.; Zou, H.; Jonzon, J.; Hummelgard, M.; Ortegren, J.; Blomquist, N.; Yang, Y.; Andersson, H.; Olsen, M.; Norgren, M.; Olin, H.; Wang, Z. L. Cellulose-Based Fully Green Triboelectric Nanogenerators with Output Power Density of 300 W m^{-2}. *Adv. Mater.* **2020**, *32*, No. e2002824.
(32) Dong, K.; Peng, X.; An, J.; Wang, A. C.; Luo, J.; Sun, B.; Wang, J.; Wang, Z. L. Shape Adaptable and Highly Resilient 3D Braided Triboelectric Nanogenerators as E-Textiles for Power and Sensing. *Nat. Commun.* **2020**, *11*, 2868.
(33) Zhang, Y.; Chen, C.; Qiu, Y.; Ma, L.; Qiu, W.; Yu, R.; Yu, W.; Liu, X. Y. Meso-Reconstruction of Silk Fibroin Based on Molecular and Nano-Templates for Electronic Skin in Medical Applications. *Adv. Fun. Mater.* **2021**, *31*, 2100150.
(34) Shen, S.; Yi, J.; Cheng, R.; Ma, L.; Sheng, F.; Li, H.; Zhang, Y.; Ning, C.; Wang, H.; Dong, K.; Wang, Z. L. Electromagnetic Shielding Triboelectric Yarns for Human-Machine Interacting. *Adv. Electron. Mater.* **2022**, *8*, 2101130.
(35) Ning, C.; Dong, K.; Gao, W.; Sheng, F.; Cheng, R.; Jiang, Y.; Yi, J.; Ye, C.; Peng, X.; Wang, Z. L. Dual-Mode Thermal-Regulating and Self-Powered Pressure Sensing Hybrid Smart Fibers. *Chem. Eng. J.* **2021**, *420*, 129650.
(36) Wang, L.; Daoud, W. A. Highly Flexible and Transparent Polyionic-Skin Triboelectric Nanogenerator for Biomechanical Motion Harvesting. *Adv. Energy Mater.* **2018**, *9*, 1803183.

https://doi.org/10.1021/acsnano.2c03365
ACS Nano XXXX, XXX, XXX−XXX

(37) Wang, Z.; An, J.; Nie, J.; Luo, J.; Shao, J.; Jiang, T.; Chen, B.; Tang, W.; Wang, Z. L. A Self-Powered Angle Sensor at Nanoradian-Resolution for Robotic Arms and Personalized Medicare. *Adv. Mater.* **2020**, *32*, No. e2001466.
(38) Peng, X.; Dong, K.; Wu, Z.; Wang, J.; Wang, Z. L. A Review on Emerging Biodegradable Polymers for Environmentally Benign Transient Electronic Skins. *J. Mater. Sci.* **2021**, *56*, 16765−16789.
(39) Sheng, F.; Yi, J.; Shen, S.; Cheng, R.; Ning, C.; Ma, L.; Peng, X.; Deng, W.; Dong, K.; Wang, Z. L. Self-Powered Smart Arm Training Band Sensor Based on Extremely Stretchable Hydrogel Conductors. *ACS Appl. Mater. Interfaces* **2021**, *13*, 44868−44877.
(40) Jing, T.; Xu, B.; Yang, Y. Organogel Electrode Based Continuous Fiber with Large-Scale Production for Stretchable Triboelectric Nanogenerator Textiles. *Nano Energy* **2021**, *84*, 105867.
(41) Jing, X.; Li, H.; Mi, H. Y.; Feng, P. Y.; Tao, X.; Liu, Y.; Liu, C.; Shen, C. Enhancing the Performance of a Stretchable and Transparent Triboelectric Nanogenerator by Optimizing the Hydrogel Ionic Electrode Property. *ACS Appl. Mater. Interfaces* **2020**, *12*, 23474−23483.
(42) Lai, Y. C.; Wu, H. M.; Lin, H. C.; Chang, C. L.; Chou, H. H.; Hsiao, Y. C.; Wu, Y. C. Entirely, Intrinsically, and Autonomously Self-Healable, Highly Transparent, and Superstretchable Triboelectric Nanogenerator for Personal Power Sources and Self-Powered Electronic Skins. *Adv. Fun. Mater.* **2019**, *29*, 1904626.
(43) Zhou, H.; Lai, J.; Jin, X.; Liu, H.; Li, X.; Chen, W.; Ma, A.; Zhou, X. Intrinsically Adhesive, Highly Sensitive and Temperature Tolerant Flexible Sensors Based on Double Network Organohydrogels. *Chem. Eng. J.* **2021**, *413*, 127544.
(44) Li, Y.; Li, X.; Zhang, S.; Liu, L.; Hamad, N.; Bobbara, S. R.; Pasini, D.; Cicoira, F. Autonomic Self-Healing of PEDOT:PSS Achieved via Polyethylene Glycol Addition. *Adv. Fun. Mater.* **2020**, *30*, 2002853.
(45) Han, L.; Liu, K.; Wang, M.; Wang, K.; Fang, L.; Chen, H.; Zhou, J.; Lu, X. Mussel-Inspired Adhesive and Conductive Hydrogel with Long-Lasting Moisture and Extreme Temperature Tolerance. *Adv. Fun. Mater.* **2018**, *28*, 1704195.
(46) Gao, Y.; Shi, L.; Lu, S.; Zhu, T.; Da, X.; Li, Y.; Bu, H.; Gao, G.; Ding, S. Highly Stretchable Organogel Ionic Conductors with Extreme-Temperature Tolerance. *Chem. Mater.* **2019**, *31*, 3257−3264.
(47) Li, Z.; Zheng, Q.; Wang, Z. L.; Li, Z. Nanogenerator-Based Self-Powered Sensors for Wearable and Implantable Electronics. *Research* **2020**, 8710686.
(48) Li, H.; Zhang, J.; Chen, J.; Luo, Z.; Zhang, J.; Alhandarish, Y.; Liu, Q.; Tang, W.; Wang, L.; Supersensitive, A. Multidimensional Flexible Strain Gauge Sensor Based on Ag/PDMS for Human Activities Monitoring. *Sci. Rep.* **2020**, *10*, 1−9.
(49) Nie, H.; Jiang, H.; Chong, D.; Wu, Q.; Xu, C.; Zhou, H. Comparison of Water Scrubbing and Propylene Carbonate Absorption for Biogas Upgrading Process. *Energy Fuels* **2013**, *27*, 3239−3245.
(50) Wang, L.; Wang, Z.; Li, Y.; Luo, Y.; Lu, B.; Gao, Y.; Yu, W.; Gao, G.; Ding, S. An Ionically Conductive, Self-Powered and Stable Organogel for Pressure Sensing. *Nanomaterials* **2022**, *14*, 714.
(51) Yu, Y.; Jin, B.; Jamil, M. I.; Cheng, D.; Zhang, Q.; Zhan, X.; Chen, F. Highly Stable Amphiphilic Organogel with Exceptional Anti-Icing Performance. *ACS Appl. Mater. Interfaces* **2019**, *11*, 12838−12845.
(52) Zhang, Y.; Tu, H.; Wu, R.; Patil, A.; Hou, C.; Lin, Z.; Meng, Z.; Ma, L.; Yu, R.; Yu, W.; Liu, X. Y. Programing Performance of Silk Fibroin Superstrong Scaffolds by Mesoscopic Regulation among Hierarchical Structures. *Biomacromolecules* **2020**, *21*, 4169−4179.
(53) Stäubli, H. U.; Schatzmann, L.; Brunner, P.; Rincón, L.; Nolte, L.-P. Mechanical Tensile Properties of the Quadriceps Tendon and Patellar Ligament in Young Adults. *Am. J. Sport. Med.* **1999**, *27*, 27−34.
(54) Lai, A.; Schache, A. G.; Lin, Y.-C.; Pandy, M. G. Tendon Elastic Strain Energy in the Human Ankle Plantar-Flexors and Its Role with Increased Running Speed. *J. Exp. Biol.* **2014**, *217*, 3159−3168.
(55) Peng, X.; Dong, K.; Ning, C.; Cheng, R.; Yi, J.; Zhang, Y.; Sheng, F.; Wu, Z.; Wang, Z. L. All-Nanofiber Self-Powered Skin-Interfaced Real-Time Respiratory Monitoring System for Obstructive Sleep Apnea-Hypopnea Syndrome Diagnosing. *Adv. Fun. Mater.* **2021**, *31*, 2103559.
(56) Zhang, B.; Yao, R.; Hu, C.; Maitz, M. F.; Wu, H.; Liu, K.; Yang, L.; Luo, R.; Wang, Y. Epigallocatechin Gallate Mediated Sandwich-Like Coating for Mimicking Endothelium with Sustained Therapeutic Nitric Oxide Generation and Heparin Release. *Biomaterials* **2021**, *269*, 120418.
(57) Zhang, B.; Qin, Y.; Yang, L.; Wu, Y.; Chen, N.; Li, M.; Li, Y.; Wan, H.; Fu, D.; Luo, R.; Yuan, L.; Wang, Y. A Polyphenol-Network-Mediated Coating Modulates Inflammation and Vascular Healing on Vascular Stents. *ACS Nano* **2022**, *16*, 6585−6597.

https://doi.org/10.1021/acsnano.2c03365
ACS Nano XXXX, XXX, XXX−XXX